Energy Advances

ROYAL SOCIETY OF CHEMISTRY

PAPER

View Article Online
View Journal



Cite this: DOI: 10.1039/d5ya00287g

# GREENcell – combination of a strain-hardened and passivated Al alloy foil anode with a F-free $LiMn_2O_4$ cathode

Kathrin Schad, *[a] Nicolas Görnert,[a] Christopher Markus Mehlich,[b] Meichen Zhan[b] and Kai Peter Birke[ab]

The rapid growth of lithium-ion battery (LiB) production calls for chemistries that combine high energy density with low environmental and economic impact. The GREENcell-concept addresses this challenge by pairing a fluorine (F)-free polyisobutylene (PIB) binder-based $LiMn_2O_4$ (LMO) cathode with an anode based on commercial aluminum (Al) alloy foil, whose theoretical capacity (993 mAh $g^{-1}$) far exceeds that of graphite (372 mAh $g^{-1}$). In this study cycling stability was improved through iterative optimization of the GREENcell-concept, targeting cathode formulation as well as Al foil composition, Al foil hardness, and Al surface passivation. Substituting polyvinylidene fluoride (PVDF)-based commercial LMO with a F-free PIB-based formulation reduced cathodic capacity fade by 17%, yet ~20% of total losses in the full-cell set up remained cathode-related. To evaluate anode optimization strategies, full-cells incorporating the F-free LMO cathode were employed. Al alloy 8011 containing iron and silicon impurities outperformed high-purity Al 1050 reference foil, improving capacity retention by ~10% through more uniform lithiation, while strain-hardened foils effectively suppressed plastic deformation compared with annealed counterparts. Surface passivation of the 8011 Al alloy foil provided further gains: a chrome(III)-based passivation improved capacity retention by 11%, and an Al silicate layer enabled the most durable cell performance, maintaining a stable capacity profile for 100 cycles after the initial losses were overcome, likely by promoting a robust solid–electrolyte interface (SEI) able to accommodate anode volume changes. Collectively, these strategies increased capacity retention after 100 cycles from 4% for uncoated annealed high-purity Al 1050 foil to 67% for the strain-hardened, Al silicate-passivated 8011 Al alloy foil, demonstrating GREENcell's promise as a scalable, low-cost, and environmentally benign LiB architecture, as demonstrated in laboratory coin cells.

Received 1st October 2025,
Accepted 14th November 2025

DOI: 10.1039/d5ya00287g

rsc.li/energy-advances



## 1. Introduction

Lithium-ion batteries (LiBs) have become indispensable for portable electronics, electric mobility, and stationary energy storage, owing to decades of continuous research and performance improvements. Today, the field faces simultaneous demands for higher energy density, lower cost, improved safety, and greater environmental sustainability. Addressing these challenges requires not only advances in materials chemistry but also innovative cell designs that combine performance with resource efficiency and industrial scalability.

A promising approach is the GREENcell-concept proposed in the previous work which integrates an *in situ* lithiated aluminum (Al) foil anode with a fluorine (F)-free spinel lithium manganese oxide (LMO, $LiMn_2O_4$) cathode.[1] LMO is composed of earth-abundant, inexpensive, and environmentally benign elements, and its compatibility with aqueous, low-cost lithium extraction methods highlights its potential as a sustainable alternative to cobalt (Co)- and nickel (Ni)-based layered oxides.[2–5] Its F-free processing further facilitates recyclability and reduces environmental impact.[6,7] However, the relatively modest capacity of LMO (~110 mAh $g^{-1}$) necessitates a high-capacity anode to achieve competitive energy density.[8,9]

Al foils provide such an opportunity. Upon initial cycling, they alloy with Li to form LiAl in a stoichiometric ratio of 1 : 1, enabling a specific capacity of ~993 mAh $g^{-1}$—substantially higher than graphite (372 mAh $g^{-1}$) and competitive with silicon (Si)/graphite (C) composites (~1138 mAh $g^{-1}$ for 20 wt% Si and 80 wt% C).[10–13] At elevated temperatures (≥60 °C), the

[a] Fraunhofer Institute for Manufacturing Engineering and Automation IPA, Nobel Str. 12, 70569 Stuttgart, Germany. E-mail: kathrin.schad@ipa.fraunhofer.de, nicolas.goernert@gmx.de, kai.peter.birke@ipa.fraunhofer.de
[b] Electrical Energy Storage Systems, Institute for Photovoltaics, University of Stuttgart, Pfaffenwaldring 47, 70569 Stuttgart, Germany. E-mail: christopher.mehlich@ipv.uni-stuttgart.de, meichen.zhan@ipv.uni-stuttgart.de, peter.birke@ipv.uni-stuttgart.de

formation of Li-rich phases ($Li_3Al_2$ and $Li_{2-x}Al$) can occur, thereby enhancing the specific capacity of the LiAl alloy to over 2000 mAh $g^{-1}$.[14,15] Zheng *et al.*[16] further reported that such Li-rich phases may also develop at room temperature under sufficiently low lithiation rates. The use of commercial Al foils eliminates the need for slurry coating, simplifies electrode processing, and leverages well-established supply chains, thereby combining performance advantages with cost efficiency and industrial viability.

Despite these advantages, severe volumetric expansion ($\sim$95%) during lithiation induces fracture, pore formation, and destabilization of the solid–electrolyte interphase (SEI), ultimately leading to continuous Li-consumption and rapid capacity fade.[12,17–19] To mitigate these degradation pathways, several electrochemical, mechanical, and chemical strategies have been proposed.

Electrochemical approaches include limiting the degree of Al utilization (DAU)—that is, restricting the fraction of Al that is lithiated—to reduce volumetric expansion while using the remaining metallic Al as a built-in current collector. Indeed, most full-cell studies that maintained >80% capacity retention beyond 100 cycles employed DAU values below 7%.[12,20–23] Alternatively, cycling restricted to the solubility range of the β-LiAl phase can limit expansion to <1.5%, though at the expense of usable capacity ($\sim$242 mAh $g^{-1}$).[20]

Mechanical strategies have focused on tuning the hardness and microstructure of Al foils. Foils with intermediate hardness (*e.g.*, Vickers hardness ($H_V$) $\sim$ 35) promote more uniform lithiation, while excessively soft ($<H_V$ 15) or hard ($>H_V$ 60) foils tend to undergo localized plastic deformation or grain fracture.[24] Improved stability with harder foils was later confirmed by Jeong *et al.*[25] identifying $H_V$ 85 as particularly promising. Multilayer laminated Al foils have also been reported to facilitate Li-diffusion and ensure anisotropic but more controlled volume expansion.[26]

Chemical modifications aim to buffer stress change and stabilize the SEI. Prelithiation, for example, can reduce polarization and alleviate stress during alloying, although it introduces additional complexity in anode handling and processing.[11,27–29] Alloying Al with active or inactive phases can also mitigate mechanical degradation. For example, incorporating inert copper (Cu) domains improved lithiation stress distribution and enabled 88% retention after 200 cycles in an lithium iron phosphate (LFP)-based full-cell.[30] Similarly, introducing 1–30 wt% Si enhanced Li-diffusion pathways and isotropic volume change, yielding more homogeneous lithiation and up to 95% retention after 100 cycles at 7 wt% Si content.[31–33] The reduced mechanical degradation observed by Crowley *et al.*[29] in Al alloys containing 1 wt% Si was attributed to changes in the grain structure, which consequently influenced the crack morphology. However, those AlSi alloys were fabricated in the lab and are not yet commercially available, limiting their immediate applicability. Artificial stabilization of the SEI has shown promising results through the implementation of passivation coatings[34,35] and modified F-rich electrolyte formulations.[36–40]

In the previous GREENcell study,[1] two stabilization strategies were particularly emphasized: (i) the use of commercial Al alloy 8011, where trace Fe (0.5–1.0 wt%) and Si (0.4–0.8 wt%) impurities enhanced stability compared to commercial high-purity Al 1050, and (ii) the application of an ion-conductive Al silicate coating, which acted as an artificial SEI precursor, reducing irreversible Li-loss. However, because alloy composition and foil temper were not independently controlled, the relative contributions of chemical composition, mechanical hardness, and surface passivation could not be distinguished. Moreover, the present study employs a different batch of alloy 8011 than previously reported, which limits direct comparison to prior results.

To address this knowledge gap, the present work systematically disentangles the specific influences of (i) Al foil composition, (ii) Al foil hardness, and (iii) surface passivation on the cycling stability of *in situ* LiAl anodes. High-purity Al 1050 and impurity-containing Al alloy 8011 were evaluated under identical temper conditions and thicknesses to decouple chemical and mechanical effects. Two passivation coatings (i) chrome (Cr)(III) and (ii) Al silicate were applied to assess their effectiveness in stabilizing the SEI and mitigating degradation. Effects of coating formulation and thickness on cycling stability are systematically investigated, and the resulting interfacial features were characterized. All experiments were performed in full-cells using an optimized F-free PIB-based LMO cathode, thereby ensuring consistency with the sustainability framework of the GREENcell-concept. A quantitative assessment of the LMO cathode's contribution to overall cell capacity loss and compares the electrochemical performance of F-free LMO cathodes with PVDF-based commercial LMO is also given.

The use of cost-efficient materials and roll-to-roll-compatible, windable cell components ensures excellent scalability and enables direct translation of the concept to commercial formats, including cylindrical cells. Benchmarking against 1050 (4% capacity retention after 100 cycles), the best-performing configuration—strain-hardened Al alloy 8011 with an Al silicate passivation coating—achieved 67% retention, a relative improvement of 63%. These findings not only clarify the specific influences of alloy composition, hardness, and surface passivation but also establish concrete design strategies for achieving stable and sustainable Al-based anodes for the GREENcell-concept as next-generation LiB.

## 2. Experimental section

### 2.1 Sample preparation

**2.1.1 Cathode preparation.** Polyisobutylene (PIB, OPPANOL® B15N and N80, BASF SE, Ludwigshafen, Germany) was employed as the F-free binder for all cell components. For this purpose, a toluene-based binder solution containing 5 wt% PIB (80 wt% B15N and 20 wt% N80) was prepared by magnetic stirring for 24 h. Two PIB-based LMO cathodes, designated LMO-1 and LMO-2, were fabricated. The LMO-1 cathode was prepared following the procedure described in the previous work[1] and consisted of 92 wt% active material, 4 wt% conductive carbon black (Super C65, Imerys S. A., Paris, France), and 4 wt% PIB binder. The LMO-2 cathode differed from LMO-1 only in the mass ratio of its constituents, comprising 90 wt%

active material, 5 wt% conductive carbon black, and 5 wt% PIB binder. The LMO active material powder ($d_{50}$ = 20–25 μm) was sourced from Lith Machine Limited (Xiamen City, China). Initially, LMO powder and Super C65 were manually premixed, followed by dispersion in toluene for 5 min. Subsequently, PIB binder was added in the form of the above-described PIB solution, and the suspension was stirred for at least 30 min. Toluene was then added to adjust the slurry to a solid content of 25–30 wt%. The slurry was coated onto Al foil (13 μm thickness, Carl Roth GmbH + Co. KG, Karlsruhe, Germany) using a doctor blade (gap size: 300 μm) and dried overnight at room temperature. Circular electrodes (Ø 16 mm) were subsequently punched out manually. For comparison with the self-fabricated PIB-based cathodes, a commercial F-containing LMO cathode using PVDF as binder was obtained from NEI Corporation (NANOMYTE® BE-35E, 100 mAh $g_{LMO}^{-1}$, $d_{50}$ = 11 μm). In the following, this commercial PVDF-based LMO cathode is referred to as LMO-Ref.

**2.1.2 Anode preparation.** Only commercially available Al foils were used in this study. High-purity Al foil 1050 (≥99.5 wt% Al) was obtained in temper conditions O and H18, with thicknesses of 30 μm and 50 μm, from LUXFOIL BÁZIS GmbH (Budapest, Hungary) and AlFiPa GmbH (Cologne, Germany). Al alloy 8011 (0.5–1.0 wt% Fe, 0.4–0.8 wt% Si) in 30 μm thickness and temper conditions O and H18 was purchased from AlFiPa GmbH. The definitions of temper conditions follow DIN EN 515:[41] O denotes fully annealed, soft material with reduced strength but enhanced formability, whereas H indicates strain-hardened material. The first digit following H specifies the processing history—"1" indicates strain hardening without subsequent thermal treatment—while the second digit specifies the tensile strength range, with "8" representing the maximum strength in the range. Two passivation strategies were applied to the Al foils. The first one, a Cr(III)-based coating (hereafter referred to as Surtec), was applied *via* a chemical process by Dittes Oberflächentechnik GmbH (Keltern, Germany). The second strategy utilized an Al silicate (AlS) coating ($K_2Al_6Si_6O_{20}(OH)_4$, $\rho$ = 2.82 g $cm^{-3}$, Irotec 8800, spherical morphology, Merck KGaA, Darmstadt, Germany), a concept introduced in the previous work.[1] This coating was prepared in two formulations: AlS1 and AlS2. For the slurry-based AlS1 coating, 96 wt% Al silicate powder was mixed with 4 wt% polyisobutylene (PIB) using the 5 wt% PIB (80 wt% B15N, 20 wt% N80) toluene solution described above. Disperbyk-161 (BYK-Chemie GmbH, Wesel, Germany) was added as a dispersing agent at 12 wt% relative to the solid fraction. Toluene was added to adjust the solid content to 53–56 wt%. The slurry was coated onto the 8011 Al alloy foil with a doctor blade (gap size: 300 μm) and dried overnight at room temperature. Disc electrodes (Ø 18 mm) were manually punched from the foils. For the AlS2 formulation, the same recipe was used without the dispersing additive, and the solid content was reduced to 35 wt%.

Additional calendered variants AlS1-k and AlS2-k were prepared by pressing the coated discs using a hydraulic lever press (manual hydraulic 15 t-press, Specac) at a load of 8 t.

Within the GREENcell anode system, the nomenclature "foil thickness–Al foil composition–temper condition|passivation coating" is used. For example, 30 μm thick Al alloy 8011 foil in temper H18 with an AlS1 coating is denoted as 30μ-8011-H18|AlS1.

An overview of all Al-based anodes used in this study is provided in Table 1. Column 5 reports the Vickers hardness ($H_V$) corresponding to the temper condition (column 3). The hardness was measured according to DIN EN ISO 6507-1[42] at the Materials Testing Institute (MPA), University of Stuttgart, using a test force of 0.15 N. For the 50 μm foils, a higher load of 0.25 N was applied due to technical limitations; this deviation is not expected to significantly affect data comparability. The hardness value for 30μ-8011-H18 is given in parentheses, as it could not be determined in full compliance with the DIN standard mentioned above due to excessive surface roughness and exhibited a high standard deviation of 5 $H_V$. Columns 6–8 of Table 1 list the alloy composition of various elements according to DIN EN 573-3,[43] with elements below 0.2% excluded. The final two columns specify the passivation coating material and thickness applied to each foil.

**2.1.3 Cell preparation.** For electrochemical characterization, both full-cells according to Fig. 1 and half-cells were assembled and tested in CR2032 coin cell format. EL-Cells®

Table 1 Overview of the Al-based anodes used in this study. The hardness of all foils was measured according to the Vickers hardness test ($H_V$, DIN EN ISO 6507-1[42]). The hardness value for Al foil 30μ-8011-H18 could not be determined in compliance with the DIN standard and is therefore given in parentheses. Columns 6–8 specify the Al foil composition of various elements in accordance with DIN EN 573-3.[43] Foreign elements with a content below 0.2 wt% were not considered. The last two columns provide details of the passivation coating applied to the Al foil, including the material type and coating thickness

| Designation | Al foil composition | Temper condition | Foil thickness μm | Foil hardness $H_V$ | Si | Fe wt% | Al | Passivation coating | Coating thickness μm |
|---|---|---|---|---|---|---|---|---|---|
| 50μ-1050-O | 1050 | O | 50 | 24 | 0.25 | 0.4 | ≥99.5 | — | — |
| 50μ-1050-H18 | 1050 | H18 | 50 | 55 | 0.25 | 0.4 | Rest | — | — |
| 30μ-1050-O | 1050 | O | 30 | 19 | 0.25 | 0.4 | Rest | — | — |
| 30μ-8011-O | 8011 | O | 30 | 16 | 0.4–0.8 | 0.5–1 | Rest | — | — |
| 30μ-8011-H18 | 8011 | H18 | 30 | (31) | 0.4–0.8 | 0.5–1 | Rest | — | — |
| 30μ-8011-H18\|Surtec | 8011 | H18 | 30 | (31) | 0.4–0.8 | 0.5–1 | Rest | Cr(III) | 3–6 |
| 30μ-8011-H18\|AlS1 | 8011 | H18 | 30 | (31) | 0.4–0.8 | 0.5–1 | Rest | Al silicate | 228 |
| 30μ-8011-H18\|AlS1-k | 8011 | H18 | 30 | (31) | 0.4–0.8 | 0.5–1 | Rest | Al silicate | 137 |
| 30μ-8011-H18\|AlS2 | 8011 | H18 | 30 | (31) | 0.4–0.8 | 0.5–1 | Rest | Al silicate | 159 |
| 30μ-8011-H18\|AlS2-k | 8011 | H18 | 30 | (31) | 0.4–0.8 | 0.5–1 | Rest | Al silicate | 99 |

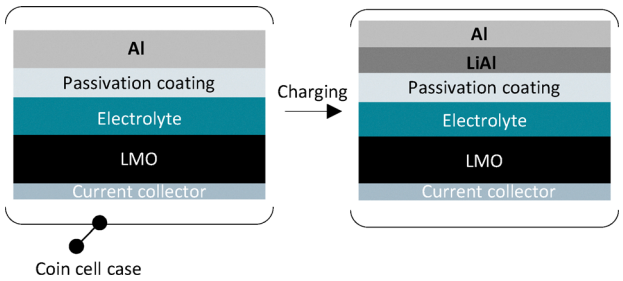


Fig. 1 Schematic representation of the GREENcell full-cell set up.

were employed for cell disassembly to enable non-destructive opening. In the full-cell configuration, a polypropylene (PP) membrane FS 2101 (0.23 mm thickness, Freudenberg Performance Materials SE & Co. KG, Weinheim, Germany) served as the separator, while a polyethylene (PE) separator (SEMCORP, 16 μm thickness) was used in the half-cell configuration. Prior to assembly, all cell components were manually punched to the required dimensions (anode: Ø 18 mm, separator: Ø 19 mm, cathode: Ø 16 mm) and dried under vacuum at 70 °C for 24 h using a vacuum oven (G-300 Drying glass oven with V-100 vacuum pump, BÜCHI Labortechnik GmbH, Essen, Germany). The electrolyte was 1 M lithium hexafluorophosphate ($LiPF_6$) in propylene carbonate (PC), supplied by E-Lyte Innovations GmbH (Kaiserslautern, Germany). Cell assembly was conducted inside an argon-filled glovebox (GS Glovebox Systemtechnik GmbH, Malsch, Germany). For half-cell measurements, the working electrodes were paired with Li metal foil (thickness 0.38 mm, as rolled 99.9%, Merck KGaA, Darmstadt, Germany).

### 2.2 Electrochemical characterization

All cell measurements were conducted using a battery tester (Arbin Instruments, College Station, TX, USA). For the full-cells a constant-current–constant-voltage (CCCV) cycling protocol was applied, beginning with a constant-current (CC) phase of ∼0.1C and a charge cut-off voltage of 4.2 V. The subsequent constant-voltage (CV) phase was terminated when the current dropped below 0.05C. After a 2 min rest period, the cells were discharged at 0.1C to a cut-off voltage of 3.1 V. All tests were carried out at 20 °C. The same cycling protocol was applied to half-cells using LMO working electrodes. The capacities of the LMO cathodes were determined separately by using the first discharge cycle capacity at a current of 50 μA. Given the iterative optimization approach of this study, the primary focus was placed on the relative optimization of the GREENcell-system. Accordingly, the relative discharge capacity was used as a key characterization parameter, calculated as the ratio of the current discharge capacity to the maximum discharge capacity after the formation cycles (first three cycles at 0.1C). Cycling data is presented as the mean values of two representative cells for each configuration. Data analysis was performed using MATLAB R2024b.

### 2.3 Material characterization

For material characterization all Al foil anodes were cycled at 0.1C as full-cells with LMO-2 as the cathode up to a defined cycle state. Cell disassembly was carried out under an argon atmosphere in a glovebox (GS Glovebox Systemtechnik GmbH, Malsch, Germany).

**2.3.1 Laser scanning microscopy.** Surface characterization of the anodes was carried out using a laser scanning microscope (LSM) (VK-X200 series, Keyence).

**2.3.2 USB camera.** To observe macroscopic morphological changes in the anodes, *ex situ* surface top view photographs were taken at defined cycling states: uncycled, 0% and 100% SOC in the 2nd formation cycle and 0% SOC after 100 cycles using a microscope camera (Digimicro mobile microscope camera, Toolcraft AG).

**2.3.3 Scanning electron microscopy.** To observe microscopic morphological changes in the anode scanning electron microscope (SEM) characterizations were employed using a JSM-IT800 (Joel, Germany). To obtain pure surface information, a low accelerating voltage of 1 kV was applied. Energy dispersive X-ray spectroscopy (EDX) mapping was conducted to enable elemental analysis using an accelerating voltage of 15 kV. Anode images were acquired as surface top views and as cross-sections at 100% SOC in the 2nd formation cycle and at 0% SOC after 100 cycles. For the preparation of foil cross-sections under vacuum, an IB-19520 Cryo Cross-Section-Polisher (CCP) (Joel, Germany) was employed. The anodes were polished along their depth using argon plasma and sample temperature control at −20 °C to prevent the sample from overheating. In the case of the AlS1 coating, parts of the layer detached during sample preparation for the CCP, resulting in only a small portion of the coating being visible in the SEM images.

## 3. Results and discussion

### 3.1 F-free cathode

To assess the performance of the F-free PIB-based LMO cathode and quantify its contribution to the overall capacity loss of the GREENcell-system, two representative formulations—LMO-1 and LMO-2—were prepared and tested in a half-cell configuration. LMO-1 contained 92 wt% active material, 4 wt% PIB-binder, and 4 wt% conductive carbon, whereas LMO-2 consisted of 90 wt% active material, 5 wt% PIB, and 5 wt% conductive carbon. The results were benchmarked against a reference PVDF-based LMO cathode, LMO-Ref, and are presented as relative discharge capacity in Fig. 2a (triangle markers) and specific discharge capacity in Fig. S1 (SI) as function of the cycle number. LMO-Ref exceeded its target capacity of 100 mAh $g_{LMO}^{-1}$ in the first cycle, achieving 102 mAh $g_{LMO}^{-1}$ (1.4 mAh $cm^{-2}$), while LMO-1 and LMO-2 both fell short of their 105 mAh $g_{LMO}^{-1}$ target with only 98 mAh $g_{LMO}^{-1}$ (0.7 mAh $cm^{-2}$) and 96 mAh $g_{LMO}^{-1}$ (0.6 mAh $cm^{-2}$) respectively (Fig. S1). LSM images (Fig. 3) reveal that the manually fabricated F-free cathodes LMO-1 (Fig. 3a) and LMO-2 (Fig. 3b) are notably more inhomogeneous than the commercial one (LMO-Ref, Fig. 3c), likely due to poorer mixing and the absence of calendering. Higher local overpotentials may further hinder active material utilization.

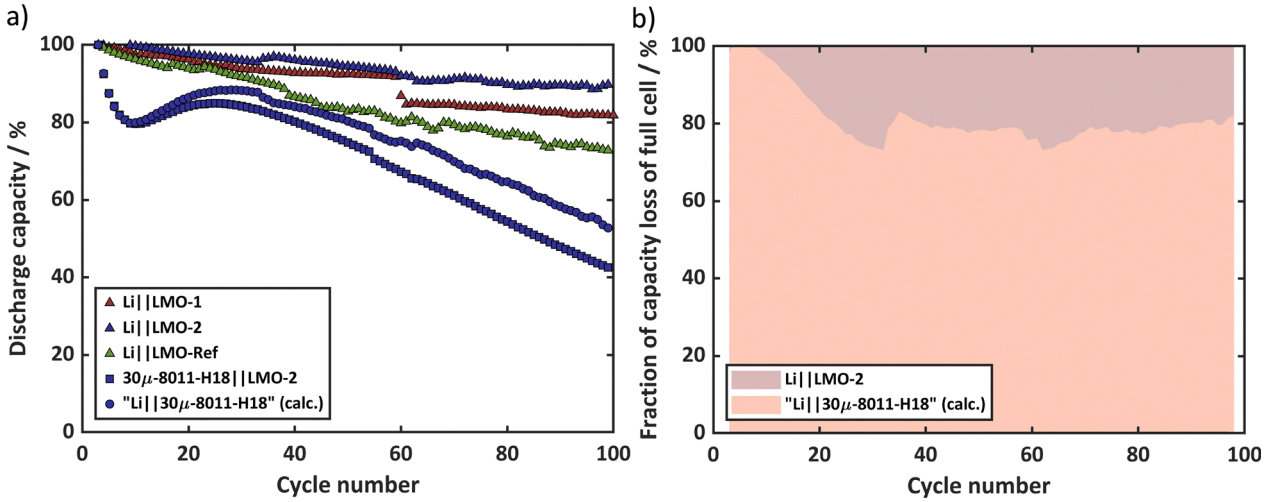


Fig. 2 Graphs for the comparison between the commercial PVDF-based LMO-cathode (LMO-Ref) and the F-free PIB-based LMO cathodes (LMO-1 and LMO-2) and comparison of the share of anode and cathode in the total ageing of the full-cell. (a) Relative discharge capacity of the cathodic half-cells (triangle marker) Li‖LMO-1, Li‖LMO-2 and Li‖LMO-Ref, the full-cell 30μ-8011-H18‖LMO-2 (square marker) and the anodic half-cell "Li‖30μ-8011-H18" (circle marker), calculated (calc.) as the difference between full-cell and cathodic half-cell, over the number of cycles. (b) Fraction of relative discharge capacity of cathode LMO-2 and 30μ-8011-H18 anode. Cycling data is presented as the mean value of two representative cells for each configuration.

Surprisingly, despite inferior coating quality, lack of calendering, and suboptimal mixing, the half-cells with the manually produced F-free cathodes LMO-1 and LMO-2 exhibited superior cycling stability compared to the PVDF-based LMO-Ref. All cathodes exhibit an approximately linear capacity fade over the course of 100 cycles (Fig. 2a, triangle markers). Among them, the PVDF-based LMO-Ref shows the lowest capacity retention, falling below 73%, indicating inferior cycling stability compared to the PIB-based variants with capacity retention above 80% after 100 cycles. Due to the large Li-reservoir on the anode side, the cathode is always fully lithiated during discharge, regardless of irreversible Li-loss to, *e.g.*, the SEI formation. Consequently, capacity fade is primarily attributed to cathode-side degradation such as particle isolation or loss of electronic contact.

These results suggest that the PIB-binder system and electrode formulation compensate for its structural drawbacks and even reduce cathodic degradation, indicating that PIB-based binders represent a viable fluorine-free alternative without compromising electrochemical performance.

Of the two F-free cathodes, LMO-2 exhibited the highest cycling stability, retaining 90% of its initial capacity (Fig. 2a, triangle markers). The improved performance compared to LMO-1 is attributed to the higher binder content, which enhances particle adhesion and promotes better mechanical integrity and electrical contact within the cathode layer. This superior coating quality is corroborated by the LSM images in Fig. 3a and b, where LMO-2 displays a more homogeneous distribution of active material compared to LMO-1. Based on its superior electrochemical stability, LMO-2 was selected as the cathode material for subsequent full-cell tests.

To quantify the contribution of cathode degradation to overall capacity fade, full-cells with the configuration 30μ-8011-H18‖LMO-2 were assembled and cycled (Fig. 2a, square markers). The corresponding relative anode half-cell capacity, calculated as the difference between the full-cell (Fig. 2a, square markers) and cathodic half-cell (Fig. 2a, triangle markers) data, is also shown in Fig. 2a (circle markers). The relative contributions of the anode and cathode to full-cell capacity fade are summarized in Fig. 2b. This comparison of the half-cell results indicates that the LMO-2 cathode contributes markedly less to the overall degradation of the full-cell than the 30μ-8011-H18 Al anode, achieving a capacity retention of 43% after 100 cycles (Fig. 2a, square markers). Initially, nearly all capacity loss can be attributed to the anode. Up to cycle 32, the relative contributions of the electrodes evolve linearly, with the cathode's impact gradually increasing (Fig. 2b). Beyond cycle 32, the degradation distribution stabilizes, with the cathode accounting for approximately 20% and the anode for 80% of the total capacity loss. These results emphasize that, although the main optimization potential resides in the anode, the cathode contribution—accounting for approximately one-fifth of the total capacity loss—remains non-negligible.

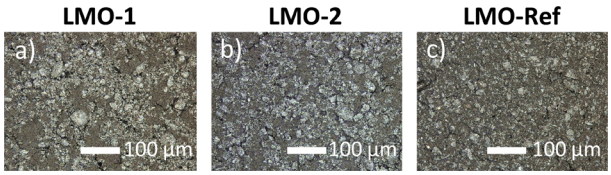


Fig. 3 LSM images of the cathode surface of (a) LMO-1, (b) LMO-2 and (c) LMO-Ref.

It should be noted, however, that the separation of anode and cathode degradation is only an approximation, since cathode half-cells were tested under Li-excess conditions and therefore do not reflect Li-losses occurring at the anode. As a result, degradation associated with progressive underlithiation of the cathode—which may trigger structural instability—is not fully captured in this assessment.

### 3.2 Al foil composition

With LMO-2 established as the cathode material, the following section investigates the influence of impurity elements present in the Al foil composition on cycling stability. To separate compositional from mechanical effects, two commercially available Al foils with identical annealed temper conditions, and foil thicknesses were selected: high-purity Al 1050-O and impurity-containing Al alloy 8011-O. The Al 1050-O is characterized by its exceptionally high purity, with a minimum Al content of 99.5 wt%, as specified in Table 1. The remaining fraction consists primarily of Si and Fe. In contrast, the 8011-O alloy contains slightly elevated levels of 0.4–0.8 wt% Si and 0.5–1.0 wt% Fe. Al foils were assembled into full-cells—denoted as 30μ-1050-O‖LMO-2 and 30μ-8011-O‖LMO-2—and evaluated by cycling tests. Fig. 4 presents the evolution of relative discharge capacity as a function of cycle number. To analyze the capacity degradation behavior, the cycling data was divided into three distinct intervals: initial capacity loss (cycles 1–5), intermediate degradation (cycles 6–30), and long-term capacity fade (cycles 30–100). Despite the relatively minor compositional differences between Al foil 1050 and Al foil 8011, their electrochemical cycling performances diverge markedly. Cells employing the high-purity 30μ-1050-O Al foil exhibit a lower initial capacity loss, retaining 92% of their capacity after five cycles, compared to 85% for cells using the 30μ-8011-O Al alloy foil. The same phenomenon is reflected by the 2% higher coulomb efficiency (CE) in cycle 5 observed for the 30μ-1050-O Al foil compared to the 30μ-8011-O Al foil (Fig. S2a, SI). This observation aligns with findings reported by Chen *et al.*[22] who compared high-purity Al (>99.99 wt% Al) with Al alloy 8111 (98.5 wt% Al, 0.61–0.64 wt% Si, 0.47–0.72 wt% Fe). The reduced initial degradation in high-purity Al is likely attributable to decreased Li-trapping, which tends to be more pronounced in alloys containing foreign elements such as Fe and Si. However, it should be noted that the exact temper conditions of the foils used by Chen *et al.*[22] are not specified, which limits the comparability of the samples.

In the intermediate cycling region (cycles 6–30), cells with the 30μ-8011-O Al alloy foil demonstrate a temporary stabilization in capacity, forming a plateau that transitions into a linear decline beginning at approximately cycle 30. In contrast, cells employing the 30μ-1050-O Al foil exhibited no such stabilization. Instead, they showed an almost exponential decline in capacity beginning around cycle 6, reaching only 4% of the initial capacity after 100 cycles. By comparison, cells with the 30μ-8011-O Al foil retained 15% of their original capacity over the same period. Fig. S2b (SI) displays the voltage profile at the onset of the charging phase. The initial peak can primarily be attributed to the combined overpotentials associated with LiAl alloy nucleation and SEI formation. For cycle 2 and 20 cycle, the peak magnitude is comparable for the 30μ-1050-O and 30μ-8011-O foils. However, by cycle 100, the peak for the 30μ-1050-O foil increases substantially relative to that of the 8011 alloy, indicating pronounced SEI growth and consequent Li-loss, assuming that the nucleation overpotential is invariant within a given foil type. These findings indicate that impurity elements such as Fe and Si exert a stabilizing effect on intermediate and long-term cycling behavior.

This interpretation aligns with the conclusions of Chen *et al.*[22] who linked the enhanced cycling performance of impurity-containing Al alloys to more uniform lithiation dynamics. It is also consistent with the work of Sharma *et al.*,[33] Xu *et al.*,[32] Tahmasebi *et al.*[31] and Crowley *et al.*,[29] who all attributed the beneficial influence of Si in Al alloys to improved Li-transport at additional phase boundaries, promoting more homogeneous lithiation and reducing mechanical degradation.

Optical images (Fig. 5a and b) provide further evidence for differences in the macrostructural morphological evolution of the 30μ-1050-O and 30μ-8011-O foils during cycling. At 0% SOC in cycle 2, a pronounced dark region is visible in the center of the 30μ-8011-O foil, suggesting localized Li-retention despite the nominally discharged state. This indicates a stronger Li-trapping tendency in the impurity-containing 30μ-8011-O alloy, whereas the feature is faint or absent in the 30μ-1050-O foil, pointing to reduced entrapment. Irreversible plastic deformation is also apparent on the back surfaces of both foils, particularly in the central region, and becomes more pronounced after lithiation to 100% SOC. Dark gray spots develop on the front side in these deformed areas, consistent with reports by Li *et al.*[24] linking such features to intensified lithiation in plastically strained regions.

Despite the early onset of deformation, the 30μ-8011-O foil shows a uniform, circular lithiation zone aligned with the cathode footprint, whereas the 30μ-1050-O foil exhibits a patchy, irregular pattern indicative of less homogeneous lithiation. After 100 cycles, both materials display substantial deformation on their reverse sides, but the 30μ-8011-O retains a relatively consistent lithiation front despite increasing brittleness, causing extensive plastic strain, and in some areas, complete rupture and holes. Collectively, these findings demonstrate that trace elements such as Fe and Si in alloy 30μ-8011-O promote more uniform lithiation and enhance long-term stability, whereas high-purity 30μ-1050-O, although favorable for the initial lithiation process, is more susceptible to mechanical degradation during prolonged cycling.

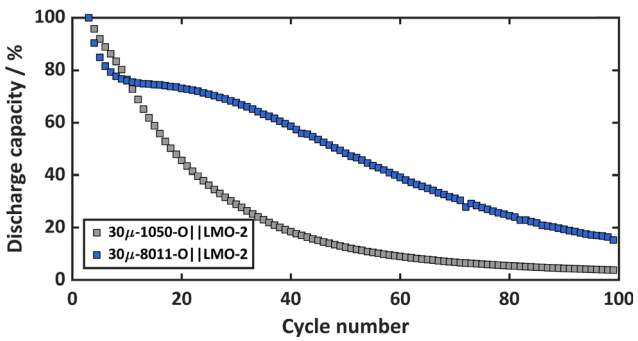


Fig. 4 Relative discharge capacity over the number of cycles using the two different Al foil compositions high-purity Al 1050 and Fe and Si containing 8011 Al alloy in the same temper condition O and thickness in the full-cell set up 30μ-1050-O‖LMO-2 *vs.* 30μ-8011-O‖LMO-2. Cycling data are presented as the mean value of two representative cells for each configuration.

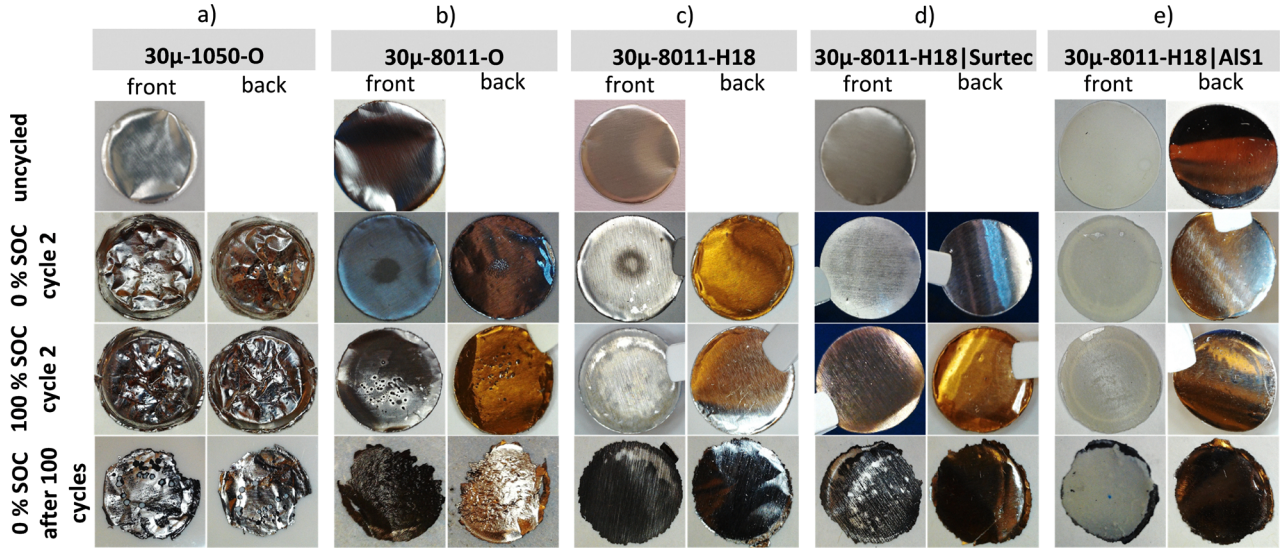


Fig. 5 Photographs of Al foils used as anode in a full-cell set up with a LMO cathode after varying cycle stages. (a) 30µ-1050-O in the cycle stages: uncycled, cycle 2 with 0% SOC, cycle 2 with 100% SOC and after 100 cycles with 0% SOC. (b) 30µ-8011-O in the cycle stages: uncycled, cycle 2 with 0% SOC, cycle 2 with 100% SOC and after 100 cycles with 0% SOC. (c) 30µ-8011-H18 in the cycle stages: uncycled, cycle 2 with 0% SOC, cycle 2 with 100% SOC and after 100 cycles with 0% SOC. (d) 30µ-8011-H18|Surtec in the cycle stages: uncycled, cycle 2 with 0% SOC, cycle 2 with 100% SOC and after 100 cycles with 0% SOC. (e) 30µ-8011-H18|AlS1 in the cycle stages: uncycled, cycle 2 with 0% SOC, cycle 2 with 100% SOC and after 100 cycles with 0% SOC.

### 3.3 Al hardness

To assess the influence of material hardness on the cycling stability of commercial Al foils, both Al 1050 and Al 8011 were examined at two distinct hardness levels. The softer variants were prepared in the annealed temper condition O, with hardness values of $H_V$ 24 for Al foil 50µ-1050-O and $H_V$ 16 for Al foil 30µ-8011-O, respectively. The harder counterparts were processed in the strain-hardened temper condition H18, exhibiting hardness values of $H_V$ 55 for Al foil 50µ-1050-H18 and $H_V$ 31 for Al foil 30µ-8011-H18, as summarized in Table 1 of the materials section. Foil thickness and chemical composition were kept constant across all sample groups to ensure consistency and allow direct comparison. Full-cells were assembled using the respective foils and PIB-based LMO-2 cathode: 50µ-1050-O‖LMO-2 and 50µ-1050-H18‖LMO-2 for high-purity Al, and 30µ-8011-O‖LMO-2 and 30µ-8011 H18‖LMO-2 for the impurity-containing Al alloy.

The evolution of relative discharge capacity with cycle number is shown in Fig. 6. For both Al 1050 and Al 8011, the strain-hardened (H18) foils exhibit superior cycling stability compared with their annealed (O) counterparts. For Al 1050, this improvement corresponds to a 7% reduction in capacity loss after 100 cycles, whereas for Al 8011 the use of the harder foil yields an even larger decrease in capacity loss of 28%.

The positive effect of sufficiently hard Al foils on long-term cycling performance has also been reported by Li *et al.*[24] and

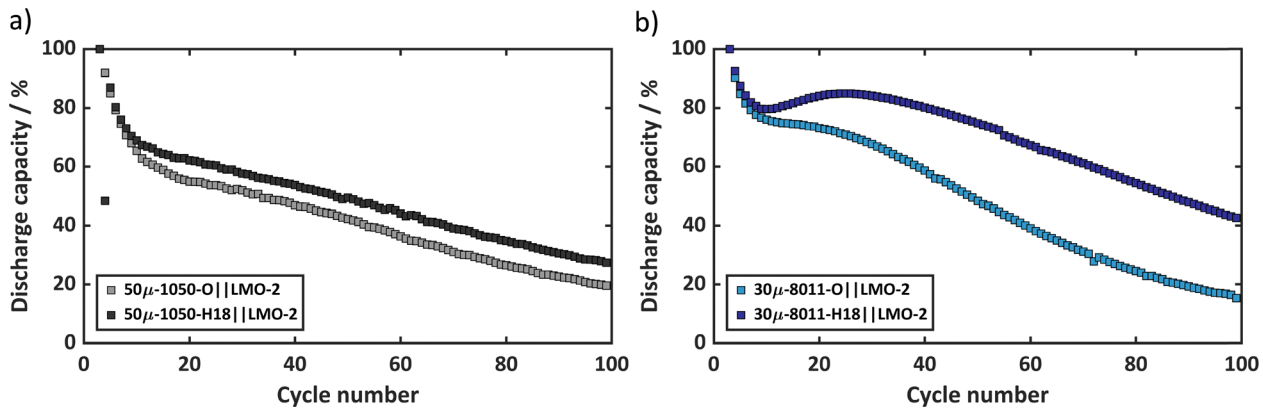


Fig. 6 Graphs for the comparison between two different hardness levels represented by the tempers annealed O and strain hardened H18 used on high-purity Al 1050 and Al alloy 8011. (a) Relative discharge capacity over the number of cycles of the full-cells 50µ-1050-O‖LMO-2 and 50µ-1050-H18‖LMO-2. (b) Relative discharge capacity over the number of cycles of the full-cells 30µ-8011-O‖LMO-2 and 30µ-8011-H18‖LMO-2. Cycling data is presented as the mean value of two representative cells for each configuration.

Jeong *et al.*,[25] who identified a minimum foil hardness of $>H_V$ 30 as critical to preventing plastic deformation of the Al matrix during lithiation. This observation is consistent with the macrostructural analysis of the Al foils 30μ-8011-O and 30μ-8011-H18 in its fully lithiated state at 100% SOC, as shown in Fig. 5b and c. In these photographs, the softer foil 30μ-8011-O exhibits clear signs of plastic deformation upon lithiation, whereas the harder foil 30μ-8011-H18 retains its mechanical integrity. This difference in mechanical behavior appears to the lithiation homogeneity as well. The softer foil 30μ-8011-O displays localized, spot-like lithiation patterns concentrated in plastically deformed regions, which contributes to severe embrittlement and continued plastic deformation after 100 cycles. In contrast, the harder foil 30μ-8011-H18 shows a much more uniform lithiation distribution at 100% SOC, with no evidence of plastic deformation even after prolonged cycling.

The embrittlement of the softer foil 30μ-8011-O results in an increased surface area, which in turn facilitates enhanced SEI formation and consequent Li-loss. This effect is corroborated by the lower CE (Fig. S3b, SI) and the higher overpotential (Fig. S3d) observed at the onset of each charging phase for the softer foil 30μ-8011-O relative to the harder counterpart 30μ-8011-H18. Based on these findings, the strain-hardened foil variant 30μ-8011-H18 emerges as a promising candidate for further development as an Al-based anode material and will serve as the reference substrate for subsequent investigations into Al passivation strategies.

### 3.4 Al passivation (SEI-precursor coating)

Despite the enhanced electrochemical performance observed in strain-hardened Al alloys incorporating alloying elements like Fe and Si, their long-term mechanical and cycling stability continues to present limitations and necessitates further improvement. The primary cause of capacity fading over extended cycling is still believed to be the embrittlement of the Al foil (Fig. 5c after 100 cycles), which leads to continuous formation of SEI layers and consequently to irreversible Li-loss and electrolyte drying.

To enhance the stability of the SEI and suppress Li-consumption, the application of ionically conductive, electrically insulating, and chemically inert passivation layers—functioning as SEI precursor coatings—was systematically investigated. Two distinct passivation strategies were examined: a Surtec coating based on Cr(III) and an Al silicate based coating (AlS) introduced in the previously published proof of concept.[1] The AlS coatings were evaluated in the two formulations AlS1 and AlS2, each analyzed in both uncalendered and calendered conditions, denoted as AlS1-k and AlS2-k, respectively. The LSM images of the passivation coatings are shown in Fig. S4 (SI).

In the previous work, the AlS coating was applied exclusively to high-purity Al foil 30μ-1050-O.[1] In the present work, this investigation is extended to evaluate the transferability and effectiveness of AlS coatings on the strain-hardened Al alloy 8011-H18 previously identified as the most promising and consistently high-performing anode foil. To evaluate the influence of the passivation coatings on cycling stability, full-cell configurations using LMO-2 cathodes were assembled and subjected to cycling tests; LMO-1 cathodes were additionally tested to evaluate transferability. All passivated anode configurations were benchmarked against a reference cell employing the uncoated Al foil 30μ-8011-H18.

The evolution of relative discharge capacity for the Surtec-passivated foils is presented in Fig. 7a. Applying the Surtec coating to the Al foil 30μ-8011-H18 enhanced cycling stability, yielding an 11% higher capacity retention after 100 cycles compared with the uncoated reference. A similar benefit was observed in full-cells paired with LMO-1 cathodes (Fig. S8a, SI). This improvement is most likely attributed to the SEI-stabilizing effect of the Surtec coating, which may also act as an artificial SEI. Within the porous coating, a stable SEI can form during the early cycles, suppressing the propagation of surface cracks in the Al foil and thereby reducing repeated SEI growth. This interpretation is supported by the evolution of the overpotential peak at the onset of the charging phase (Fig. 8c). While the uncoated Al foil 30μ-8011-H18 exhibited a steadily increasing voltage peak with cycle number, indicative of continuous SEI

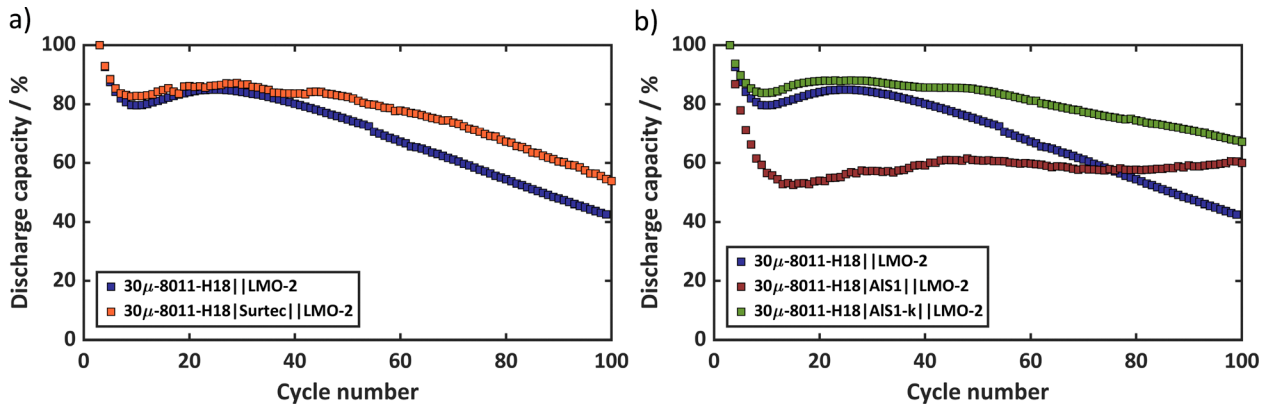


Fig. 7 Graphs for the analysis of the influence of using an inert, ion conducting passivation layer coated on the Al foil. The full-cell set up 30μ-8011-H18‖LMO-2 is used as reference. (a) Relative discharge capacity over the number of cycles of the full-cell using a Cr(III) passivation coating (Surtec): 30μ-8011-H18|Surtec‖LMO-2. (b) Relative discharge capacity over the number of cycles of the full-cells using an uncalendered Al silicate (AlS) and a calendered Al silicate (AlS-k) coating: 30μ-8011-H18|AlS1‖LMO-2, 8011-H18|AlS1-k‖LMO-2. Cycling data is presented as the mean value of two representative cells for each configuration.

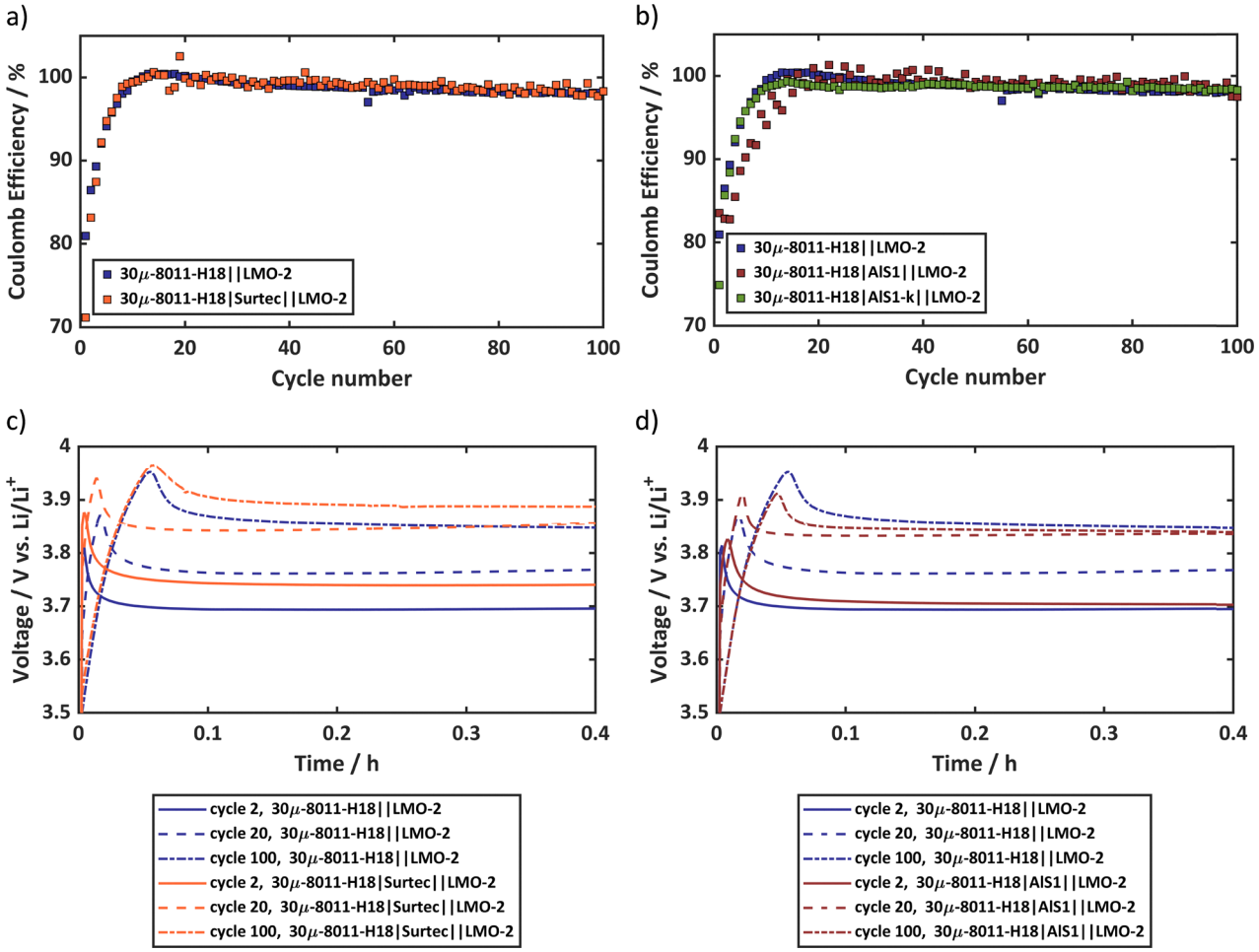


Fig. 8 Graphs for the analysis of the influence of using an inert, ion conducting passivation layer coated on the Al foil. The full-cell set up 30μ-8011-H18‖LMO-2 is used as reference. (a) Coulomb efficiency over the number of cycles of the full-cell using a Cr(III) passivation coating (Surtec): 30μ-8011-H18|Surtec‖LMO-2. (b) Coulomb efficiency over the number of cycles of the full-cells using an uncalendered Al silicate (AlS) and a calendered Al silicate (AlS-k) coating: 30μ-8011-H18|AlS1‖LMO-2, 8011-H18|AlS1-k‖LMO-2. (c) Voltage profiles at the onset of the charging phase of cycle 2, cycle 20 and cycle 100 over time of the full-cell using a Cr(III) passivation coating (Surtec). (d) Voltage profile at the onset of the charging phase of cycle 2, cycle 20 and cycle 100 over time of the full-cell using an uncalendered Al silicate (AlS).

growth, the coated foil 30μ-8011-H18|Surtec showed a markedly mitigated overpotential growth, reflecting suppressed SEI evolution at extended cycle numbers.

Evidence for this mechanism is provided by the SEM images and EDX mappings in Fig. 9. For the uncoated 30μ-8011-H18 anode, large surface cracks are visible in the Al foil in the second charging cycle at 100% SOC (Fig. 9a and b). These cracks deepen with extended cycling to 100 cycles (Fig. 9d and e) and appear in cross-section as craters and voids (Fig. 9g). The resulting increase in surface area promotes SEI growth and Li-trapping, accelerating Li-loss. EDX maps (Fig. 9c and f), showing F-enrichment, further confirm extensive SEI growth along crack surfaces. In contrast, the Surtec-coated anode 30μ-8011-H18|Surtec retains a smooth, almost crack-free surface at both 100% SOC in cycle 2 and 0% SOC in cycle 100 (Fig. 9h and k), indicating uniform lithiation and consistent with the macroscopic observations in Fig. 5d.

After 100 cycles, the cross-section shown in Fig. 9n reveals that structural deformation within the lithiation area is markedly reduced, and the SEI remains more evenly distributed compared to the uncoated version (Fig. 9m *vs.* Fig. 9f). Collectively, these findings confirm that the Surtec passivation coating enhances SEI stability and preserves the structural integrity of the Al anode during prolonged cycling.

The evolution of relative discharge capacity for the AlS1 passivation coatings is shown in Fig. 7b. When using the uncalendered AlS1 coating, the discharge capacity declined rapidly to 54% within the first ten cycles but subsequently stabilized, yielding a capacity retention of 60% after 100 cycles—an improvement of ~20% compared with the uncoated 30μ-8011-H18 foil.

Liang *et al.*,[35] and Ling *et al.*[34] have attributed such benefits of passivation coatings to their ability to stabilize the SEI, enhance ionic conductivity, and promote a more uniform electrolyte distribution at the electrode–electrolyte interface. This argumentation aligns with the results of the previous work.[1] A pronounced initial capacity loss associated with porous passivation layers has also been noted by Ling *et al.*[34]

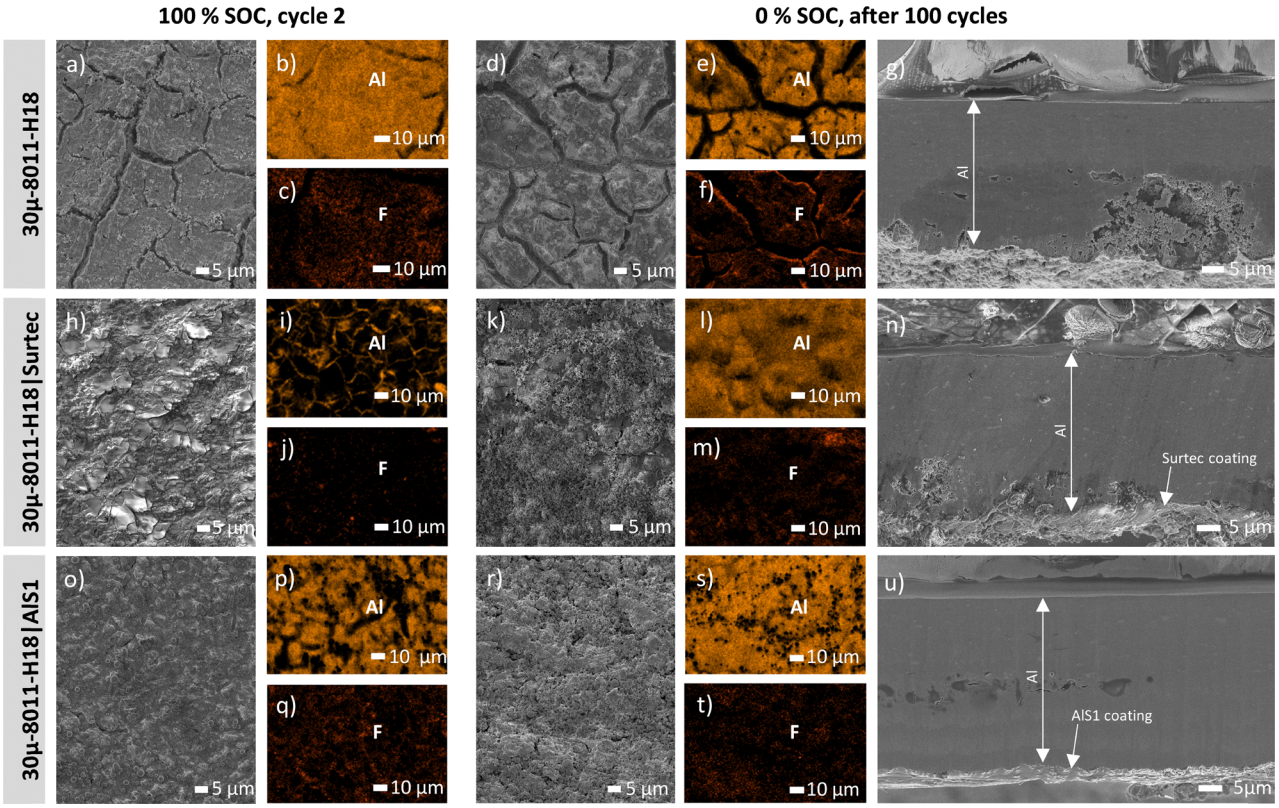


Fig. 9 Surface top-view and cross-section SEM images and EDX mappings of uncoated and coated Al foils used as anode in a full-cell set up with LMO-2 cathode after the cycle stages 100% SOC in cycle 2 and 0% SOC after 100 cycles. In the case of cross-sectional images, the lithiated side of the Al foil is at the lower edge of the foil. (a)–(f) Surface top view SEM images and EDX mapping of 30µ-8011-H18. (g) Cross-section SEM image of 30µ-8011-H18. (h)–(m) Surface top view SEM image and EDX mapping of 30µ-8011-H18|Surtec. (n) Cross-section SEM image of 30µ-8011-H18|Surtec. (o)–(t) Surface top view SEM image and EDX mapping of 30µ-8011-H18|AlS1. (u) Cross-section SEM image of 30µ-8011-H18|AlS1. Complete EDX mappings and cross-sectional SEM images of the anodes at 100% SOC in the second cycle are shown in Fig. S5–S7 (SI).

The high porosity of the uncalendered AlS1 coating likely facilitates extensive electrolyte infiltration, accelerating Li-consumption during SEI formation in the early cycles. This interpretation is supported by the comparatively narrower LiAl phase observed in the fully lithiated AlS1-coated foil (Fig. S7a *vs.* Fig. S5a in SI), suggesting that a significant fraction of Li is consumed within the porous layer.

By contrast, the calendered variant 30µ-8011-H18|AlS1-k and the uncoated reference 30µ-8011-H18 retained >80% of their initial capacity after ten cycles (Fig. 7b). Despite its lower initial loss, the 30µ-8011-H18|AlS1-k foil exhibited a steeper decline over extended cycling, implying that a minimum level of porosity is necessary to maintain SEI stability. Even so, the reduced early loss enabled the 30µ-8011-H18|AlS1-k foil to retain 67% of its capacity after 100 cycles—an improvement of 27% relative to the uncoated baseline. The evolution of the CE further supports these observations (Fig. 8b). The CE of the coated, uncalendered variant 30µ-8011-H18|AlS1 remained below that of the uncoated reference 30µ-8011-H18 up to approximately the 20th cycle but consistently surpassed it thereafter, apart from minor fluctuations. This transition indicates that, after the initial SEI formation, further degradation processes are effectively suppressed by the AlS1 passivation layer, signifying the development of a stable and mechanically robust SEI.

This interpretation is further corroborated by the evolution of the overpotential peak at the onset of the charging phase (Fig. 8d). For the uncoated reference 30µ-8011-H18, the overpotential peak increased progressively with cycle number, reflecting continuous SEI growth even at advanced cycling stages. In contrast, the overpotential of the coated variant 30µ-8011-H18|AlS1 increased only until approximately the 20th cycle and then remained constant up to 100 cycles, confirming the establishment of a stable SEI.

Passivation with the thinner AlS2 coating also enhanced cycling stability (Fig. S8b, SI). For both the uncalendered 30µ-8011-H18|AlS2 and calendered 30µ-8011-H18|AlS2-k anode variants, capacity loss after 100 cycles was reduced by more than 10% compared with bare foil. In this case, the influence of porosity on initial and long-term behavior was negligible, as the discharge profiles of AlS2 and AlS2-k were nearly identical. This response is consistent with the substantially lower thickness of AlS2, which likely minimizes porosity-related effects observed in the thicker AlS1 layer.

Macroscopic and microscopic post-cycling analyses confirm the protective role of AlS coatings (Fig. 5e and 9o–u). At 100%

SOC in cycle two, AlS1-coated foils exhibit a uniform lithiated zone, and after 100 cycles they show markedly less pulverization than uncoated references (Fig. 5e, 9o, r, u, Fig. S5a and b). Cross-sectional image in Fig. 9u reveals an absence of surface cracks, while the EDX map of F in Fig. 9t demonstrates a more homogeneous SEI distribution compared to the uncoated foil 30μ-8011-H18 (Fig. 9f), indicating that the AlS1 layer promotes formation of a mechanically resilient interphase capable of accommodating the volumetric changes of Al during cycling.

Overall, these findings demonstrate that passivation of Al-foil anodes with either Surtec or AlS coatings substantially improves long-term cycling stability. They also extend the positive effects presented in the previously work[1] for AlS-coated 30μ-1050-O foils to 30μ-8011-H18 Al substrates. Among all tested coatings, the uncalendered variant 30μ-8011-H18|AlS1 emerges as the most promising, being the first to sustain a stable discharge-capacity profile for 100 cycles once the initial loss is surpassed. This behavior suggests that the thicker, more porous layer facilitates the formation of a robust, stable SEI capable of accommodating the anode's volumetric changes during cycling. Nevertheless, the pronounced early-cycle capacity loss remains a limitation; future work should focus on optimizing coating thickness and porosity to minimize initial Li-consumption while preserving the long-term stability benefits demonstrated by AlS1.

## 4. Conclusion

This study demonstrates that the GREENcell-concept—combining a commercial Al alloy foil anode with a F-free LMO cathode—can be substantially optimized through careful control of cathode chemistry, Al foil composition, foil hardness, and surface passivation. Replacing PVDF-based commercial LMO with a F-free formulation reduced the cathodic contribution to capacity fade, though cathode degradation, accounting for approximately 20% of overall losses, remains non-negligible. On the anode side, a commercially available 8011 Al alloy containing Fe and Si impurities outperformed high-purity Al 1050, improving capacity retention by ∼10% due to more uniform lithiation dynamics, while strain-hardened foils (H18, $H_V \sim 31$–$55$) proved essential for preventing plastic deformation during cycling and enhancing homogenous lithiation compared with soft annealed variants. Al passivation further enhanced performance: the Cr(III)-based coating Surtec improved capacity retention after 100 cycles by 11%, and the uncalendered Al silicate coating AlS1 emerged as the most effective measure, sustaining a stable discharge profile for up to 100 cycles once its initial capacity loss was overcome, likely by supporting the formation of a robust SEI that accommodates anode volume changes. Collectively, these measures increased the relative discharge capacity after 100 cycles from 4% using the untreated high-purity 30μ-1050-O Al reference foil to 67% using the strain-hardened AlS1-k passivated 30μ-8011-H18|AlS1-k foil, demonstrating the strong potential of the GREENcell-concept as a sustainable, low-cost, and durable battery concept. Future improvements should focus on minimizing the initial Li loss by optimizing coating thickness and porosity, tailoring the electrolyte composition, and identifying the optimal concentration of impurity elements such as Si in the Al alloy to further enhance cycling stability. Extending these strategies to scalable formats such as cylindrical cells could pave the way for the GREENcell-concept to become a commercially viable, low-cost, and environmentally sustainable battery platform.

## Author contributions

The manuscript was written through contributions of all authors. Conceptualization, K. S.; methodology, K. S.; investigation, K. S.; experimental investigation, K. S., N. G., C. M. M. and M. Z.; data curation and analysis, K. S. and N. G.; resources, K. S. and K. P. B.; writing – original draft preparation, K. S.; writing – review and editing, N. G., K. P. B., C. M. M. and M. Z.; visualization, K. S.; supervision, K. P. B.; project administration, K. S.; funding acquisition, K. P. B. and K. S. All authors have given approval to the final version of the manuscript.

## Conflicts of interest

There are no conflicts to declare.

## Data availability

The rest of the data can be provided with reasonable request. The data that support the findings of this study is shown in supplementary information (SI). Supplementary information is available. See DOI: https://doi.org/10.1039/d5ya00287g.

## Acknowledgements

The authors acknowledge financial support by the Ministry of Economic Affairs, Labor and Tourism in Baden-Württemberg (project "SEEDBattery" funding code BW1_1208/02). The authors acknowledge the help of Serdar Seymen and Alexander Fill in the early stages of this study.

## References

1 K. Schad, D. Welti and K. P. Birke, Proof of Concept: The GREENcell—A Lithium Cell with a F-, Ni- and Co-Free Cathode and Stabilized In-Situ LiAl Alloy Anode, *Batteries*, 2023, **9**, 453, DOI: 10.3390/batteries9090453.
2 X. Zhao, Y. Gong, K. Gao, Y. Wang and H. Y. Yang, Tailored LMO@COF composite electrodes for direct electrochemical lithium extraction from high-temperature brines, *Chem. Eng. J.*, 2023, **474**, 145975, DOI: 10.1016/j.cej.2023.145975.
3 X. Zhao, Y. Wang, Y. Wang, H. Zhang, Z. Zhao, L. Zhu and Y. Wang, Integrating flexibility and lattice engineering in Al Br Co-doped self-supporting LiMn2O4 electrodes for efficient lithium extraction, *Chem. Eng. J.*, 2025, **521**, 166575, DOI: 10.1016/j.cej.2025.166575.
4 X. Zhao, L. Zheng, Y. Hou, Y. Wang and L. Zhu, Pulsed electric field controlled lithium extraction process by LMO/

MXene composite electrode from brines, *Chem. Eng. J.*, 2022, **450**, 138454, DOI: 10.1016/j.cej.2022.138454.
5 Z. Zhao, Y. Wang, H. Guo, L. Gan, Y. Wang and X. Zhao, A truncated octahedral Li-rich LiMn2O4 electrode for long-life electrochemical lithium extraction from brine, *Nano Mater. Sci.*, 2025, DOI: 10.1016/j.nanoms.2024.08.004.
6 M. Weijers, P. Karanth, J. Borninkhof and F. M. Mulder, Fluorine-Free Lithium-Ion Batteries: A Working Alternative, *Batteries Supercaps*, 2025, e202500469, DOI: 10.1002/batt.202500469.
7 E. K. Savvidou, A. Rensmo, J. P. Benskin, S. Schellenberger, X. Hu, M. Weil and I. T. Cousins, PFAS-Free Energy Storage: Investigating Alternatives for Lithium-Ion Batteries, *Environ. Sci. Technol.*, 2024, **58**, 21908–21917, DOI: 10.1021/acs.est.4c06083.
8 Y. Miao, P. Hynan, A. von Jouanne and A. Yokochi, Current Li-Ion Battery Technologies in Electric Vehicles and Opportunities for Advancements, *Energies*, 2019, **12**, 1074, DOI: 10.3390/en12061074.
9 B. E. Murdock, K. E. Toghill and N. Tapia-Ruiz, A Perspective on the Sustainability of Cathode Materials used in Lithium-Ion Batteries, *Adv. Energy Mater.*, 2021, **11**, 2102028, DOI: 10.1002/aenm.202102028.
10 H. Wang, H. Tan, X. Luo, H. Wang, T. Ma, M. Lv, X. Song, S. Jin, X. Chang and X. Li, The progress on aluminum-based anode materials for lithium-ion batteries, *J. Mater. Chem. A*, 2020, **8**, 25649–25662, DOI: 10.1039/d0ta09762d.
11 S. Chen, X. Yang, J. Zhang, J. Ma, Y. Meng, K. Tao, F. Li and J. Geng, Aluminum–lithium alloy as a stable and reversible anode for lithium batteries, *Electrochim. Acta*, 2021, **368**, 137626, DOI: 10.1016/j.electacta.2020.137626.
12 T. Zheng and S. T. Boles, Lithium aluminum alloy anodes in Li-ion rechargeable batteries: Past developments, recent progress, and future prospects, *Prog. Energy*, 2023, **5**, 032001, DOI: 10.1088/2516-1083/acd101.
13 D. Karabelli and K. P. Birke, Feasible Energy Density Pushes of Li-Metal *vs.* Li-Ion Cells, *Appl. Sci.*, 2021, **11**, 7592, DOI: 10.3390/app11167592.
14 T. Zheng, J. Zhang, W. Jin and S. T. Boles, Utilization of Li-Rich Phases in Aluminum Anodes for Improved Cycling Performance through Strategic Thermal Control, *ACS Appl. Energy Mater.*, 2023, **6**, 1845–1852, DOI: 10.1021/acsaem.2c03673.
15 M. Z. Ghavidel, M. R. Kupsta, J. Le, E. Feygin, A. Espitia and M. D. Fleischauer, Electrochemical Formation of Four Al-Li Phases (β-AlLi, Al 2 Li 3, AlLi 2−x, Al 4 Li 9) at Intermediate Temperatures, *J. Electrochem. Soc.*, 2019, **166**, A4034–A4040, DOI: 10.1149/2.0061916jes.
16 T. Zheng, J. Zhang, X. Guo, W. Jin and S. T. Boles, Unlocking room temperature formation of Li-rich phases in aluminum anodes for Li-ion batteries, *Electrochim. Acta*, 2024, **485**, 144127, DOI: 10.1016/j.electacta.2024.144127.
17 W.-J. Zhang, A review of the electrochemical performance of alloy anodes for lithium-ion batteries, *J. Power Sources*, 2011, 13–24, DOI: 10.1016/j.jpowsour.2010.07.020.
18 W. J. Jeong, C. Wang, S. G. Yoon, Y. Liu, T. Chen and M. T. McDowell, Electrochemical behavior of elemental alloy anodes in solid-state batteries, *ACS Energy Lett.*, 2024, **9**, 2554–2563, DOI: 10.1021/acsenergylett.4c00915.
19 Y. Liu, C. Wang, S. G. Yoon, S. Y. Han, J. A. Lewis, D. Prakash, E. J. Klein, T. Chen, D. H. Kang and D. Majumdar, *et al.*, Aluminum foil negative electrodes with multiphase microstructure for all-solid-state Li-ion batteries, *Nat. Commun.*, 2023, **14**, 3975, DOI: 10.1038/s41467-023-39685-x.
20 T. Zheng, D. Kramer, R. Mönig and S. T. Boles, Aluminum Foil Anodes for Li-Ion Rechargeable Batteries: the Role of Li Solubility within β-LiAl, *ACS Sustainable Chem. Eng.*, 2022, **10**, 3203–3210, DOI: 10.1021/acssuschemeng.1c07242.
21 B. Ji, F. Zhang, M. Sheng, X. Tong and Y. Tang, A Novel and Generalized Lithium-Ion-Battery Configuration utilizing Al Foil as Both Anode and Current Collector for Enhanced Energy Density, *Adv. Mater.*, 2017, **29**, 1604219, DOI: 10.1002/adma.201604219.
22 T. Chen, A. C. Thenuwara, W. Yao, S. E. Sandoval, C. Wang, D. H. Kang, D. Majumdar, R. Gopalaswamy and M. T. McDowell, Benchmarking the Degradation Behavior of Aluminum Foil Anodes for Lithium-Ion Batteries, *Batteries Supercaps*, 2023, **6**, e202200363, DOI: 10.1002/batt.202200363.
23 C. Trejo, K. Scanlan and A. Manthiram, Impact of LiAl Nucleation Kinetics on the Microstructural Evolution of Aluminum Foil Anodes in Lithium-ion Batteries, *J. Electrochem. Soc.*, 2024, **171**, 40539, DOI: 10.1149/1945-7111/ad3ec2.
24 H. Li, T. Yamaguchi, S. Matsumoto, H. Hoshikawa, T. Kumagai, N. L. Okamoto and T. Ichitsubo, Circumventing huge volume strain in alloy anodes of lithium batteries, *Nat. Commun.*, 2020, **11**, 1584, DOI: 10.1038/s41467-020-15452-0.
25 H. T. Jeong and W. J. Kim, Electrochemical performance of high-hardness high-Mg aluminum alloy foils as negative electrodes for lithium-ion batteries, *J. Alloys Compd.*, 2025, **1016**, 178962, DOI: 10.1016/j.jallcom.2025.178962.
26 J. Li, S. Sun, X. Zhang and G. Wang, Laminated Aluminum Foil Anode for Lithium-Ion Batteries, *ACS Appl. Energy Mater.*, 2025, **8**, 3826–3836, DOI: 10.1021/acsaem.5c00068.
27 J. Ryu, J. Kang, H. Kim, J. H. Lee, H. Lee and S. Park, Electrolyte-mediated nanograin intermetallic formation enables superionic conduction and electrode stability in rechargeable batteries, *Energy Storage Mater.*, 2020, **33**, 164–172, DOI: 10.1016/j.ensm.2020.08.012.
28 Y. Yu, S. Li, H. Fan, H. Xu, M. Jiang, Y. Huang and J. Li, Optimal annealing of Al foil anode for prelithiation and full-cell cycling in Li-ion battery: The role of grain boundaries in lithiation/delithiation ductility, *Nano Energy*, 2020, **67**, 104274, DOI: 10.1016/j.nanoen.2019.104274.
29 P. J. Crowley, K. P. Scanlan and A. Manthiram, Diffusional lithium trapping as a failure mechanism of aluminum foil anodes in lithium-ion batteries, *J. Power Sources*, 2022, **546**, 231973, DOI: 10.1016/j.jpowsour.2022.231973.
30 M. Zhang, L. Xiang, M. Galluzzi, C. Jiang, S. Zhang, J. Li and Y. Tang, Uniform Distribution of Alloying/Dealloying Stress for High Structural Stability of an Al Anode in High-Areal-Density Lithium-Ion Batteries, *Adv. Mater.*, 2019, **31**, e1900826, DOI: 10.1002/adma.201900826.
31 M. H. Tahmasebi, D. Kramer, H. Geßwein, T. Zheng, K.-C. Leung, B. T. W. Lo, R. Mönig and S. T. Boles, In situ formation of aluminum-silicon-lithium active materials in

aluminum matrices for lithium-ion batteries, *J. Mater. Chem. A*, 2020, **8**, 4877–4888, DOI: 10.1039/c9ta13745a.

32 C. Xu, Y. Wang, S. Sun, S. King, M. S. Kurbanov, X. Zhang and G. Wang, Competitive Lithiation Mechanism of Silicon in Aluminum–Silicon Alloy Foil Anodes for Lithium-Ion Batteries, *ACS Sustainable Chem. Eng.*, 2024, **12**, 17018–17025, DOI: 10.1021/acssuschemeng.4c07331.

33 S. S. Sharma, P. J. Crowley and A. Manthiram, Aluminum–Silicon Alloy Foils as Low-Cost, Environmentally Friendly Anodes for Lithium-Ion Batteries, *ACS Sustainable Chem. Eng.*, 2021, **9**, 14515–14524, DOI: 10.1021/acssuschemeng.1c05168.

34 H. Y. Ling, Z. Su, H. Chen, L. Hencz, M. Zhang, Y. Tang and S. Zhang, Biomass-Derived Poly(Furfuryl Alcohol)–Protected Aluminum Anode for Lithium-Ion Batteries, *Energy Technol.*, 2019, **7**, 1800995, DOI: 10.1002/ente.201800995.

35 X. Liang, Y. Yang, X. Jin, Z. Huang and F. Kang, The high performances of $SiO_2/Al_2O_3$-coated electrospun polyimide fibrous separator for lithium-ion battery, *J. Membr. Sci.*, 2015, 1–7, DOI: 10.1016/j.memsci.2015.06.016.

36 B. S. Parimalam and B. L. Lucht, Reduction Reactions of Electrolyte Salts for Lithium Ion Batteries: LiPF 6, LiBF 4, LiDFOB, LiBOB, and LiTFSI, *J. Electrochem. Soc.*, 2018, **165**, A251–A255, DOI: 10.1149/2.0901802jes.

37 X. Ou, G. Zhang, S. Zhang, X. Tong and Y. Tang, Simultaneously pre-alloying and artificial solid electrolyte interface towards highly stable aluminum anode for high-performance Li hybrid capacitor, *Energy Storage Mater.*, 2020, **28**, 357–363, DOI: 10.1016/j.ensm.2020.03.021.

38 X. Zhang, W. Zhao, J. Cai, C. Xu, S. Chen, G. Chen and G. Wang, Solid electrolyte interphase layer induced electrochemical behavior diversity of aluminum foil anode for lithium ion batteries, *Solid State Ionics*, 2022, **387**, 116081, DOI: 10.1016/j.ssi.2022.116081.

39 X. Liu, Q. Zhu, A. Jiang, J. Yue, D. Yu, S. Wang, S. Dong, J. Zhao, W. Wang and S. Lyu, *et al.*, Realizing a Wide-Temperature Aluminum-Foil-Anode-Based Lithium-Ion Battery, *Adv. Funct. Mater.*, 2025, e21637, DOI: 10.1002/adfm.202521637.

40 X. Gu, J. Dong and C. Lai, Li-containing alloys beneficial for stabilizing lithium anode: A review, *Eng. Rep.*, 2021, **3**, e12339, DOI: 10.1002/eng2.12339.

41 Deutsches Institut für Normung e. V. EIN EN 515: Aluminium und Aluminiumlegierungen – Halbzeug – Bezeichnungen der Werkstoffzustände, 2017.

42 Deutsches Institut für Normung e. V. DIN EN ISO 6507-1: Metallische Werkstoffe DIN EN ISO 6507-1: Metallische Werkstoffe – Härteprüfung nach Vickers – Teil 1: Prüfverfahren, 2024.

43 Deutsches Institut für Normung e. V. DIN EN 573-3: Aluminium und Aluminiumlegierungen – Chemische Zusammensetzung und Form von Halbzeug, 2022.